Journal of Nuclear Materials 407 (2010) 10–15

Contents lists available at ScienceDirect

Journal of Nuclear Materials

journal homepage: www.elsevier.com/locate/jnucmat

Lattice strain and damage evolution of 9–12%Cr ferritic/martensitic steel during *in situ* tensile test by X-ray diffraction and small angle scattering

Xiao Pan [a], Xianglin Wu [a], Kun Mo [a], Xiang Chen [a], Jonathan Almer [b], Jan Ilavsky [b], Dean R. Haeffner [b], James F. Stubbins [a,*]

[a] Department of Nuclear, Plasma and Radiological Engineering, University of Illinois at Urbana-Champaign, Urbana, IL 61801, USA
[b] Advanced Photon Source, Argonne National Laboratory, Argonne, IL 60439, USA

A B S T R A C T

In situ X-ray diffraction and small angle scattering measurements during tensile tests were performed on 9–12% Cr ferritic/martensitic steels. The lattice strains in both particle and matrix phases, along two principal directions, were directly measured. The load transfer between particle and matrix was calculated based on matrix/particle elastic mismatch, matrix plasticity and interface decohesion. In addition, the void or damage evolution during the test was measured using small angle X-ray scattering. By combining stress and void evolution during deformation, the critical interfacial strength for void nucleation was determined, and compared with pre-existing void nucleation criteria. These comparisons show that models overestimate the measured critical strength, and require a larger particle size than measured to match the X-ray observations.

© 2010 Published by Elsevier B.V.

1. Introduction

Damage initiation or void nucleation of structural steels has always been a topic of considerable technological importance and scientific interest. It has received extensive attention motivated by the need to enhance damage tolerance and avoid fracture in structural materials. During the last three decades, several initiation criteria were developed to predict the onset of damage by particle/matrix debonding [1–3]. These models were divided into different classes depending on the energy or stress/strain calculation. The most common criteria are stress criterion and strain criterion [4]. Although most of these models were in agreement with the experimental results, most of the 3D-based criteria calculations were derived from 2D experimental observations by *ex situ* SEM tensile tests [5,6]. The experimental characterization is based on post-deformation (static) microstructural characterization which contains no information about the dynamic processes involved in the evolution of failure. No literature existed to directly measure the local critical strain or critical stress between particle and matrix during void nucleation.

With development of new technology, X-ray tomography [7–9] was used to observe the void nucleation in 3D during *in situ* tests. The damage evolution, together with effect of matrix hardness and particle volume fraction, was carried out at each deformation step visually on the 3D region. Based on the 3D experimental observation and finite element modeling, strain and stress criteria to characterize the particle/matrix debonding were investigated. Results show that stress criteria have higher Weibull modulus than strain criteria [8]. While this analysis of damage initiation in metallic materials using 3D X-ray tomography represents a significant breakthrough, it does not take into account the chemical reactions between the particles and the matrix, i.e. interface strength between particle and matrix. Another limitation confining the application of X-ray tomography is that the resolution of tomography is only about 1 μm; however in most cases, the size of carbide in structural materials is in the range of 0.01–1 μm so that X-ray tomography cannot precisely detect the onset of void nucleation in carbon steel. High-energy X-ray diffraction provides a unique and advanced method to directly measure the lattice strains between particle and matrix for various crystallographic orientations during *in situ* tensile tests. The stress or load transfer between particle and matrix can be calculated directly based on matrix/particle elastic mismatch, matrix plasticity, interface decohesion and even particle fracture. In addition, the void or damage evolution during the test can be measured by small angle X-ray scattering simultaneously with X-ray diffraction. Taken together, these methods lend insight into mechanisms controlling void nucleation.

2. Experimental procedure

Four types of simplified ferritic/martensitic model alloys were selected for this study. These model alloys are based on the Fe–Cr–C composition produced by Carpenter Technology Corporation.

* Corresponding author. Tel.: +1 217 3336474; fax: +1 217 3332906.
E-mail address: jstubbin@illinois.edu (J.F. Stubbins).

0022-3115/$ - see front matter © 2010 Published by Elsevier B.V.
doi:10.1016/j.jnucmat.2010.07.003

The nominal chemical compositions of four types of model alloys are Fe–9%Cr–0.1%C, Fe–9%Cr–0.5%C, Fe–12%Cr–0.2%C, and Fe–12%Cr–0.5%C respectively. The concentrations of Cr in model alloys are very similar with modified 9Cr–1Mo (T91) and HT9, which are the promising candidates for advanced reactor systems including the fusion reactor (ITER) and accelerator-based neutron systems (SNS) due to their high performance at elevated temperature, low thermal stress and low liquid metal corrosion rates [10,11]. Thus, the results from this work will also offer valuable insights into these alloys. In addition, different heat treatments were applied to each type of model alloy to get distinct particle sizes and distributions, thus effect of particle characters can be analyzed thoroughly. The results from Fe–9%Cr–0.5%C are presented here.

High energy X-ray diffraction measurements were carried out at the 1-ID beamline of the Advanced Photon Source (APS) in Argonne National Laboratory. *In situ* uniaxial tensile tests were performed on a MTS closed-loop servo-hydraulic test frame under displacement control. Flat SS-3 type tensile samples with nominal gage length of 7.62 mm, width of 1.52 mm and thickness of 0.76 mm were used during the tensile test. All tensile tests were conducted at a crosshead speed of 0.005 mm/s, corresponding to an initial specimen strain rate of 10^{-3} per second. More details of experimental setup and X-ray diffraction analysis can be found in Ref. [12].

The damage evolution during the *in situ* tensile test was measured by small angle X-ray scattering (HE-SAXS) simultaneously using the same setup as X-ray diffraction. The Q range of HE-SAXS is from 0.035 to 1.3 $Å^{-1}$. The size of particle or void which can be distinguished is down to 5 nm. The resolution is much higher than the traditional SEM measurement and tomography. *Ex situ* ultra small-angle X-ray scattering (USAXS) studies were also conducted at Sector 32ID of the APS. USAXS uses single crystal optics to extend the dynamic Q-vector range to lower values compared to standard (pinhole) SAXS instruments and makes it possible to measure features up to 1 μm in size [13,14]. The USAXS instrument has a large dynamic Q range from 0.0003 $Å^{-1}$ up to 1 $Å^{-1}$, limited due to strength of scattering from these samples up to about 0.04 A^{-1}. Several selected samples, such as untested samples, tested sample with some strain levels, and fractured samples, were carried out. Small pieces (1.5 × 4 mm) were cut from tested samples along the loading direction, then mechanically polished down to 30–40 μm.

The void evolution was also locally examined *ex situ* using a JEOL 6060LV Scanning Electron Microscope (SEM) on selected tested samples after being subjected to various strain levels.

3. Results

3.1. Void evolution

The damage evolution during the *in situ* tensile test was measured by small angle X-ray scattering. As shown in Fig. 1, the calibrated scattering intensity increases with deformation, and then jumps up quickly especially after reaching the ultimate tensile strength (UTS) level. Although other features, such as dislocations and second phases, can contribute to the scattering intensity, the main contribution is from the presence of voids due to their relatively high contrast factor [15]. Fig. 2 shows results fit to Porod's law [16,17] of Fe–9%Cr–0.5%C–16d alloy tested at room temperature:

$$I = Aq^{-4} + B \tag{1}$$

where I is calibrated scattering intensity, q is scattering vector, and A is proportional to the specific surface area of the scatterer center. Since voids mainly contribute to the increasing scattering intensity, increases in A are attributed to increases in their specific surface area and assuming similar size and shape, to their void fraction. It is clear that there are no measurable voids nucleated in the elastic region. Once the deformation passes the yield point, a small number of voids start to nucleate. The voids nucleate continuously as the strain increases. This continuous void nucleation is related to the complex local conditions around the particles, which involves the particle size, particle shape, particle distribution. Thus the critical nucleation condition for different particles is achieved at a variety of strain levels. Although certain types of voids start to nucleate upon yielding, the void density up to UTS (22.5%) is still low. The low-void-density tail at small strain is attributed to Type I particles,

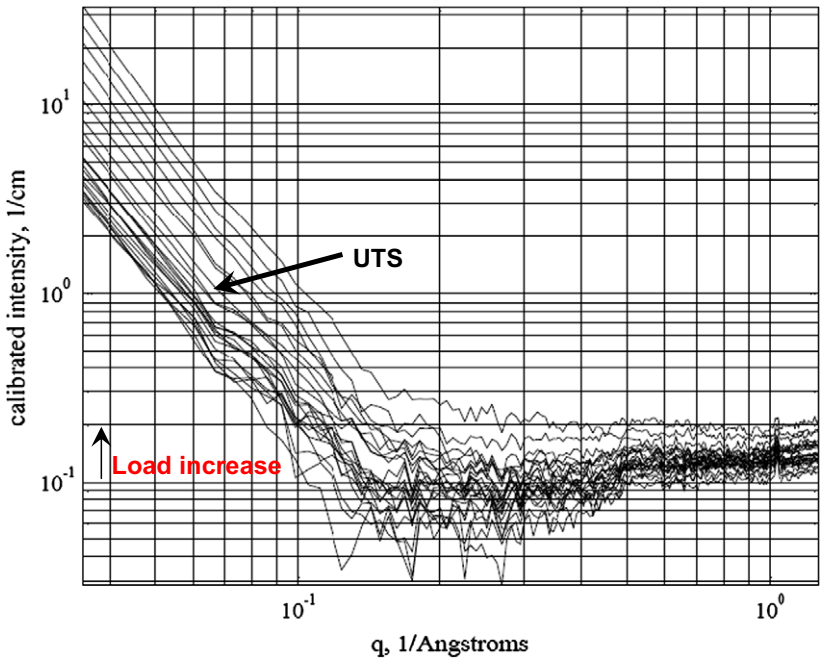

Fig. 1. SAXS profiles of Fe–9%Cr–0.5%C–16d tested at room temperature.

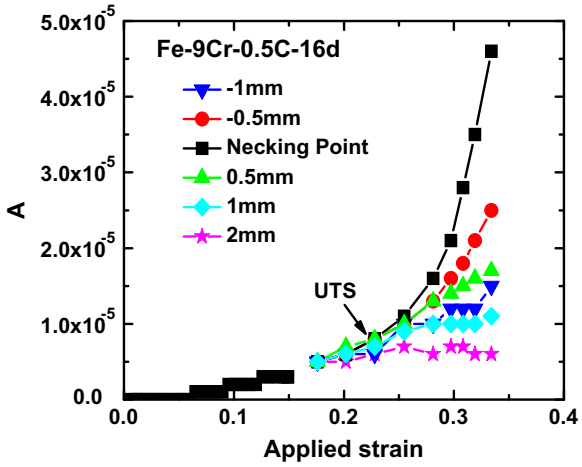

Fig. 2. Porod A vs. applied strain for Fe–9%Cr–0.5%C–16d tested at room temperature.

such as irregular shape particles, extra large particle with defects, and particle clusters [18]. Kwon and Asaro [18] systematically investigated void nucleation at low strain range and found that three types of particles contribute to low strain void nucleation, i.e. large inclusions, large elongated particles, and closely spaced particles. They classified those particles into Type I particles. Further investigation on the Type I particles illustrated that void density from Type I particles increases rapidly within a narrow strain level and saturates at a well-defined threshold value until fracture. The SEM picture taken right at UTS is shown in Fig. 3a. It can be seen that the most of the voids are associated with debonding around larger particles, cracking of irregular shape particles, or separation of two close particles, marked with A and B. The remaining particles are still perfectly bonded with the matrix. Here a similar idea is used to categorize the voids into two types. Type I voids include the cracking of irregular shape particles, separation between closely spaced particles or particle cluster, large particle with defects. Type II void nucleation is characterized by interfacial debonding around normal carbide particles with a specific size distribution. In the following sections, the void nucleation refers to Type II if there is no additional explanation.

It is shown from Fig. 2 that the void density starts to rise dramatically at or around the necking center after passing the UTS. In Fig. 2 black line with rectangular shape stands for the necking point during the test, i.e. $Y = 0$, and other color lines stands for several measuring points away from the necking point with some distance along the loading direction. With increasing distance from necking center, the void density decreases correspondingly, for example $Y = \pm 0.5$ mm. At locations far away from the necking center, i.e. $Y = 2$ mm, the void density almost remains at similar levels as that at the UTS. Fig. 3b shows the void behavior close to the necking center just passed the UTS ($\varepsilon = 0.35$). The void density increases but is still low. And most of voids are around the large particles. Some of the voids have already grown in some extent with cylindrical shape. By comparing the void evolution right at and after UTS, it is still hard to determine when the void starts to nucleate since the true plastic strain increases significantly even with a small amount of necking. The cylindrical shape of void indicates that it nucleated in a strain level earlier than 0.35. As opposed to the detailed microscopic observations, the *in situ* void observations using HE-SAXS are inherently more statistically-relevant. The void density distribution along the loading direction is rather uniform before UTS, and Type I voids dominate. After passing UTS, the void density distribution becomes inhomogeneous. The rapid increase of the void density in the vicinity of the neck is due to the development of a triaxial stress state in this region, which promotes and accelerates void nucleation and growth. In regions far away from the necking center, the strain stays at a similar level as that at UTS. This points to the UTS as the critical point for void nucleation. The stress on the particle at UTS is the critical interfacial stress for large particle. Once the void nucleation occurs, the void keeps growing. Babout et al. [7] discovered that there is no growth threshold once the void initiation point is reached. This is consistent with the cylindrical void shape as shown in Fig. 3b.

Fig. 3c shows another SEM pictures at a higher applied strain of $\varepsilon = 0.55$. The voids initiating early around large particles continue to grow, and some voids start to nucleate around particles with smaller size. It is interesting to notice that most of the voids are concentrated around the large particles. The voids associated with the small particles are also close to the large particles. Once the large particles start to debond, principally along the loading direction, they carry less load, which is primarily transferred to smaller particles in their vicinity. Thus the critical condition for void nucleation is easier to reach for the small particles around the large particles where the voids have already nucleated. With further strain, these large voids start to link together by themselves or by the small voids associated with small particles surrounding them. Once more and more voids link together, internal cracks start to form, ultimately leading to fracture. This fracture process is called void sheet coalescence, which has already been investigated extensively [4].

3.2. Lattice strain and stress analysis

The detailed results of lattice strain evolution were reported in a previous paper [12]. In summary, the response of lattice plane strain in ferrite can be divided into three stages, namely the elastic, grain to grain yield, and stage III. Fig. 4 shows the axial lattice strain vs. applied strain for matrix and particle of Fe–9%Cr–0.5%C–16d tested at room temperature. There is no lattice strain mismatch between particle and matrix during elastic region, after passing the yield point, the load starts to transfer from matrix to particle. Materials deform uniformly up to UTS. Once passing the UTS point, necking starts to occur so that plastic deformation localizes in the necking region. Once the axial (ε_{22}) and transverse (ε_{11}) lattice strain of an *hkl* peak from a given diffraction peak are measured from peak shifts, the internal stress on the particle can be analyzed by Young et al. [19]:

$$\sigma_{22} = \frac{E}{1+\nu}\varepsilon_{22} + \frac{\nu E}{(1+\nu)(1-2\nu)}(\varepsilon_{22}+\varepsilon_{11}+\varepsilon_{33})$$
$$\sigma_{11} = \sigma_{33}\frac{E}{1+\nu}\varepsilon_{11} + \frac{\nu E}{(1+\nu)(1-2\nu)}(\varepsilon_{11}+\varepsilon_{22}+\varepsilon_{33}) \quad (2)$$

where σ_{22} is axial principle stress, σ_{11} and σ_{33} are transverse principle stress. E_{hkl} and ν_{hkl} from experiment are used for each (*hkl*) reflection. High energy X-ray diffraction can directly measure the elastic strain on the particles. Through strain and stress analysis on the particle using Eq. (2), the stress evolution during the tensile test can be evaluated. The internal stress behavior shows similar response as lattice strain as shown in Fig. 2, i.e. the internal stress increases with increasing of applied strain uniformly up to the UTS. After passing the UTS, the stress shows scattered behavior.

4. Discussion

4.1. Damage evolution and ductile fracture process

Ductile fracture is a mode of material failure comprised of three stages: void nucleation, growth and coalescence. It has already been shown that inclusions or second phase particles play an

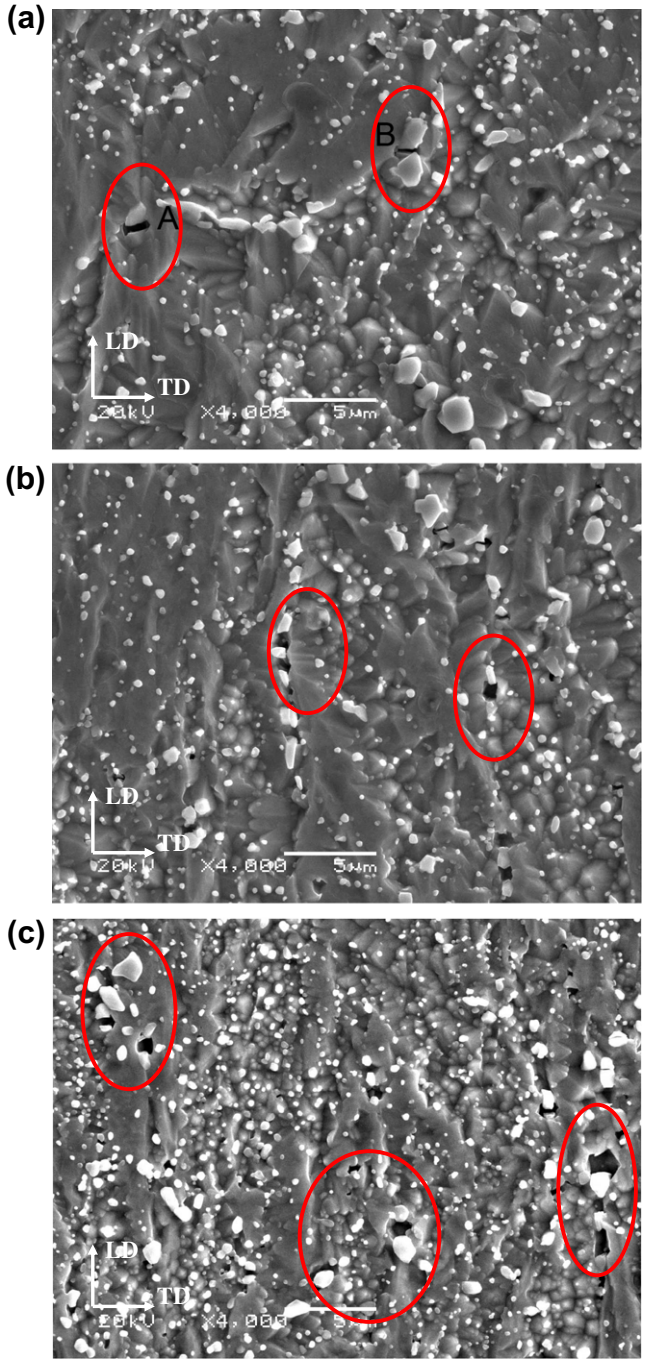

Fig. 3. Void evolution of Fe–9%Cr–0.5%C–16d at different plastic deformation steps: (a) UTS, $\varepsilon = 0.225$, (b) $\varepsilon = 0.35$, and (c) $\varepsilon = 0.55$.

important role in ductile fracture, especially in void nucleation, or damage initiation [4,5]. Void nucleation is the first step of the ductile fracture, and usually it is induced by interfacial debonding between particle and matrix or particle cracking. Research has also shown that void nucleation is a complex process since void nucleation depends on the local environment of each particle [4]. Void nucleation has received extensive attention motivated by the need to enhance damage tolerance and avoid fracture in structural materials. However, most of experimental characterization is based on post-deformation (static) microstructural characterization which contains no information about the dynamic processes involved in the evolution of failure. Furthermore, the systematical uncertainty of extrapolation cannot provide the right information

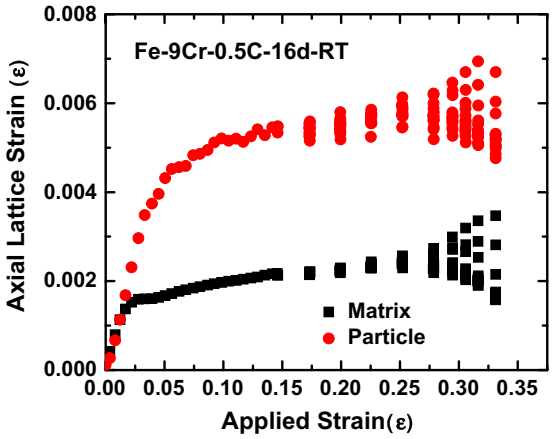

Fig. 4. Axial lattice strain vs. applied strain for matrix and particle of Fe–9%Cr–0.5%C–16d tested at room temperature.

on the void nucleation strain, the key parameter in the modeling analysis. Kwon and Asaro [18] reported that the different extrapolation methods influence the accuracy of the critical interfacial strength. Although it is more accurate to determine the void nucleation strain for regular particles by considering the effect of Type I particles than the traditional extrapolation procedure, systematic uncertainties due to resolution limitations of SEM still exist. In addition, mechanical polishing during the sample preparation can induce damage and bias the quantitative analysis [20].

The results in this paper suggest that UTS is a critical point for void nucleation of large particles existing in a semi-bimodal size-distributed system. Before the UTS, the critical void nucleation condition is not reached, so void nucleation only occurs around Type I particles. Once passing the UTS, the critical condition occurs and voids start to nucleate more generally. For a given particle size distribution, the voids nucleate at large particles first in some preferred locations. This is because the plastic relaxation of large particles is more difficult [12,18], or because larger particles have low interfacial strength between the particle and matrix so that it is easy to trigger void nucleation [21]. Although the large particles only account for a small percentage of the total particles, the loss of load due to interfacial separation is significant. So the load re-distributes to the surrounding, which leads to the rupture of the matrix that has already deformed plastically. If it happens that there are many more debonded large particles horizontally in a region, material cannot carry more load and necking starts to occur in that region. It is believed that the onset of necking, or end of uniform elongation is associated with the load re-distribution due to debonding of large particles. Once necking starts, the hydrostatic tension stress due to triaxial stress is developed, which enhances and expedites the void nucleation process for all size of particles. This is consistent with the dramatic increase in void density around the necking center as observed by HE-SAXS. Although the void growth is not the focus of this study, the cylindrical shape of voids from SEM microstructural picture indicates that the void simultaneously start to grow once they nucleate. No threshold for void growth has also been reported by Babout et al. [7].

The void density around the necking center is much higher than the other places along the loading direction. The void density decreases correspondingly with distance between the measurement point and necking center. Fig. 5 shows the intensity as function of scattering vector q of Fe–9%Cr–0.5%C–4d tested at room temperature measured by USAXS at sector 32 in APS [1](green line: initial

[1] For interpretation of color in Figs. 1–5, the reader is referred to the web version of this article.

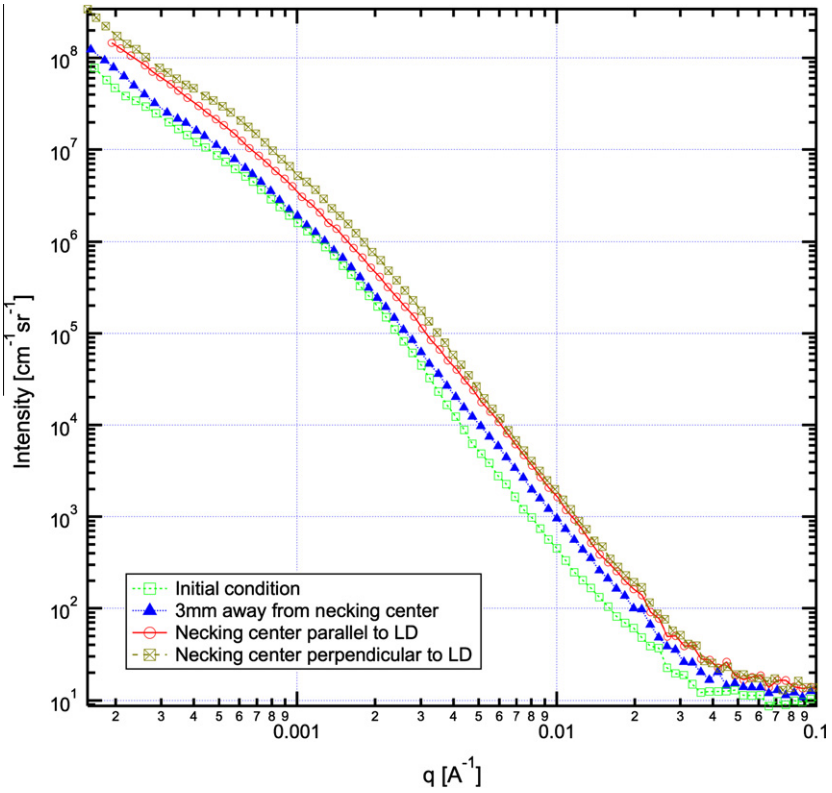

Fig. 5. USAXS data of Fe–9%Cr–0.5%C–4d alloy (fracture sample).

condition referred as reference condition; red line: at necking center and scattering vector is parallel to the loading direction; gray line: at necking center and scattering vector is perpendicular to the loading direction; blue line: 3 mm away from necking center along loading direction). Higher intensity stands for higher density of features, such as voids and particles, being scattered by X-rays. The void density at the necking center is much higher than that at 3 mm away from the necking center, while the void density remains low at the point 3 mm away from the necking center. Although USAXS and HE-SAXS cover different q-value ranges, the voids evolution has the same behavior: void density around the necking center is always larger than elsewhere. The position dependency of void density just matches the critical stress criterion. At the necking center, strong hydrostatic tension stress is developed due to the triaxial stress from complex geometry of necking center as shown Fig. 6. The hydrostatic stress and true strain were calculated by following equations:

$$\sigma_h = (\sigma_{11} + \sigma_{22} + \sigma_{33})/3$$
$$\varepsilon_t = 2\ln(t_0/t)$$

where t_0 is initial sample thickness, and t is real sample thickness during the test. The hydrostatic tensile stress increases linearly with true strain. The influence of hydrostatic tension stress has been investigated by Kwon and Asrao [18]. They found that the void nucleation strain in the notched specimen is lower than that in smooth specimen. By applying a hydrostatic stress, the critical interfacial stress is easier to reach so that the void nucleates earlier. The effect of a hydrostatic stress on void nucleation has also reported by French and Weinrich [22] and Chen [23]. In addition, Fig. 5 also shows the difference of void density measured with diffraction vector parallel and perpendicular to the loading direction. It is interesting to investigate the inhomogeneity of the necking deformation in the future, which might have influence on the void growth and coalescence.

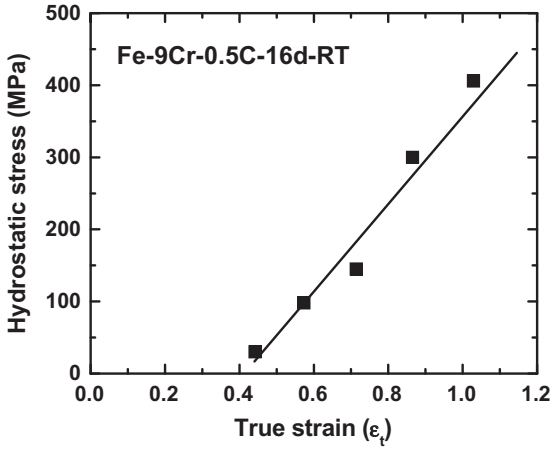

Fig. 6. Hydrostatic tensile stress vs. true strain in Fe–Fe–9%Cr–0.5%C–16d alloy.

With increasing hydrostatic stress, more and more particles satisfy the critical stress criterion and start to nucleate. It is interesting to note that most voids nucleating later around smaller particles are close to the large particles that have already debonded. This phenomenon is associated with load re-distribution because the particles lose the partial load-carrying capacity once void nucleation occurs. With further straining, the voids around the large particles become linked or link up with the small voids around them, and finally the material fails. From above discussion, damage initiation starts from large particles, then those voids continuously grow and new voids occur around the small particles, and finally voids around large particle link together by themselves or assisting with small voids. Although the large particles only account for the small percentage of the total particle numbers, they play a vital role on the whole ductile fracture process.

Table 1
Comparison of critical interfacial strength of Fe–9%Cr–0.5%C alloys tested at room temperature for three heat treatments.

Interfacial strength	Fe–9%Cr–0.5%C–4d	Fe–9%Cr–0.5%C–8d	Fe–9%Cr–0.5%C–16d
This work	1162	1120	1065
Dislocation model (r = average size)	1490 (r = 0.2 μm)	1426 (0.23 μm)	1344 (0.26 μm)
Dislocation model (r = larger size)	1089 (0.4 μm)	1044 (0.4 μm)	921 (0.5 μm)

4.2. Critical stress criterion

When the stress on the particle/matrix interface is larger than the critical interfacial strength, voids nucleate. Void nucleation strain depends on the stress state, but the interfacial strength of particle is a material constant. The evaluation of the interfacial strength can be carried out by continuum analysis, dislocation models and fracture analysis [1–5,18]. Although most of these models were in agreement with the experimental results, most of the 3D-based criteria calculations were derived from 2D experimental observations by *ex situ* SEM tensile tests. Furthermore, all of the proposed models simplify the derivation by considering the uniform distribution of particle or by simplifying the particle shapes. High-energy X-ray diffraction technology provides unique and advanced method to directly and continuously measure the lattice strains between particle and matrix for various crystallographic orientations during *in situ* tensile tests. As discussed above, void starts to nucleation once the UTS is reached. At that point, void nucleation only occurs around the large particles in each size distribution, and most of particles are still well bonded. So the internal stress on the particle is the critical interfacial strength for large particles, not for average size particles.

The comparison of critical interfacial strength between calculation by direct lattice strain measurement (σ_{22} in Eq. (2)) and indirect calculation based on the micro-mechanism of dislocation behavior near particles, i.e. the dislocation model, is listed in Table 1. The dislocation model is expressed as:

$$\sigma_{\text{interfacial}} = 4.48\times10^{-3}r^{-0.7}(\varepsilon_n)^{0.3} + 1.75\times10^{-2}\mu(\varepsilon_n/r)^{0.5} + \sigma_T/(1-f_v)$$

Detailed derivation is reviewed in Kwon and Asrao [18]. Here r is particle radius, ε_n is the true void nucleation strain, σ_T is the triaxial stress and f_v is the void volume fraction. It can be seen that the modeling prediction is higher than the calculation by direct lattice strain measurement. The difference comes from the particle size used in the dislocation model. In the dislocation model, the average particle size is used, while calculation with direct lattice strain measurement just catches the void nucleation around the large particle. Table 1 also shows the critical interfacial strength by replacing average particle size with larger particle size for three alloys. It is obvious that the critical interfacial strength decreases to the same stress level as calculation from direct X-ray measurement. The model evaluation using larger particle size is very close to the calculation from strain measurement, which indicates that the dislocation model can predict the critical interfacial strength very well. It has already been shown that the main deformation mechanism in these types of simplified model alloys is dislocation accumulation and annihilation [24,25]. Thus the dislocation model based on the dislocation interaction can describe the critical interfacial strength reasonably well. This result also agrees with Thomason's argument that the dislocation model is valid when the particle radius is smaller than 1 μm [26]. This result also indicates that interfacial strength has size dependence, the critical interfacial strength for average size is higher than that of the large particle.

In addition, most of previous prediction of critical interfacial strength for spheroidized steels with carbide diameters ranging between 0.02 and 1 μm is around 1000–2000 MPa [27]. Those predictions also are closed to direct calculation from the lattice strain measurement here. Basically, the model prediction of critical interfacial strength is valid and consistent with the experiments.

5. Conclusions

In situ tensile test of model alloys were performed at different temperatures using high-energy X-ray scattering. The lattice strain evolution was measured using wide-angle scattering, while void nucleation was tracked using small angle scattering. The following conclusions could be drawn:

1. The UTS is a critical and starting point for void nucleation. Void nucleation occurs first around large particles in each particle distribution after passing UTS, and then extends to smaller particles.
2. Lattice strain and void density variations along the specimen gauge length are associated with localized deformation after necking.
3. The void nucleation and associated values for interfacial strengths can be predicted from the dislocation model using larger particle size, which matches the X-ray measurement. Using the known average particle size leads to an overestimation of the critical interfacial strength.

Acknowledgements

The work was supported by the US Department of Energy Under Grants DE-FC07-051D14665, DE-FG07-02D14337, and (APS) under DE-AC02-06CH11357.

References

[1] S.H. Goods, L.M. Brown, Acta Metall. 27 (1979) 1–15.
[2] K. Tanaka, T. Mori, T. Nakamura, Philos. Mag. 21 (1970) 267.
[3] M.F. Ashby, Philos. Mag. 14 (1966) 1157.
[4] W.M. Garrison, N.R. Moody, J. Phys. Chem. Solids 48 (1987) 1035–1074.
[5] H. Qiu, H. Mori, M. Enoki, T. Kishi, ISIJ Int. 39 (1999) 358–364.
[6] J.B. Kosco, D.A. Koss, Metall. Trans. A 24 (1993) 681–687.
[7] L. Babout, E. Maire, J.Y. Buffiere, R. Fougeres, Acta Mater. 49 (2001) 2055–2063.
[8] L. Babout, E. Maire, R. Fougeres, Acta Mater. 52 (2004) 2475–2487.
[9] L. Babout, Y. Brechet, E. Maire, R. Fougeres, Acta Mater. 52 (2004) 4517–4525.
[10] S.A. Maloy, M.R. James, W.R. Johnson, T.S. Byun, K. Farrell, M.B. Toloczko, J. Nucl. Mater. 318 (2003) 283–291.
[11] T.S. Byun, K. Farrell, E.H. Lee, J.D. Hunn, L.K. Mansur, J. Nucl. Mater. 298 (2001) 269–279.
[12] X. Pan, X. Wu, X. Chen, K. Mo, J. Almer, D.R. Haeffner, J.F. Stubbins, J. Nucl. Mater. 398 (2009) 220–226.
[13] A. Hammons, W. Wang, J. Ilavsky, M.L. Pantoy, B.L. Weeks, M.W. Vaughn, Phys. Chem. Chem. Phys. 10 (2008) 193–199.
[14] J. Ilavsky, P.R. Jemian, A.J. Allen, F. Zhang, L.E. Levine, G.G. Long, J. Appl. Cryst. 42 (2009) 469–479.
[15] G.G. Long, L.E. Levine, R.J. Fields, Mater. Sci. Eng. A 309–310 (2001) 28.
[16] G. Porod, Kolloid Z. Z. Polym. 124 (1951) 83–114.
[17] G. Porod, Kolloid Z. Z. Polym. 125 (1952) 108–122.
[18] D. Kwon, R.J. Asaro, Metall. Trans. 21A (1990) 117.
[19] M.L. Young, J.D. Almer, M.R. Daymond, D.R. Haeffner, D.C. Dunand, Acta Mater. 55 (2007) 1999–2011.
[20] E. Maire, C. Bordreuil, L. Babout, J. Boyer, J. Mech. Phys. Solids 53 (2005) 2411–2434.
[21] I. Sabirov, D. Duschlbauer, H.E. Pettermann, O. Kolednik, Mater. Sci. Eng. A 393 (2005) 275–285.
[22] I.E. French, D.F. Weinrich, Scripta Metall. 8 (1974) 87.
[23] C.W. Chen, Acta Metall. 9 (1961) 68.
[24] R. Bonade, P. Spatig, M. Victoria, T. Yamamoto, G.R. Odette, J. Nucl. Mater. 329–333 (2004) 278–282.
[25] R. Bonade, P. Spatig, R. Schaublin, M. Victoria, Mater. Sci. Eng. A 387–389 (2004) 16–21.
[26] P.F. Thomason, Ductile Fracture of Metals, Pergamon Press, Oxford, 1990.
[27] D. Kwon, Scripta Metall. 22 (1988) 1161–1164.